Optimization of the Bias Magnetic Field of Shear Wave EMATs

Julio Isla and Frederic Cegla

Abstract— **The main advantage of electromagnetic acoustic transducers (EMATs) over piezoelectric transducers is that no direct contact with the specimen under test is required. Therefore, EMATs can be used to test through coating layers. However, they produce weaker signals, and hence, their design has to be optimized. This paper focuses on the design of a Lorentz force shear wave EMAT and its application in thickness gaging; special emphasis is placed on the optimization of the design elements that correspond to the bias magnetic field of the EMAT. A configuration that consists of several magnets axisymmetrically arranged around a ferromagnetic core with like poles facing the core was found to give the best results. By using this configuration, magnetic flux densities in excess of 3 T were obtained in the surface of a specimen; the maximum value achieved by a single magnet under similar conditions is roughly 1.2 T. If the diameter of an EMAT ultrasonic aperture is 10 mm, the proposed configuration produces signals roughly 20 dB greater than a single magnet, while for a given overall EMAT volume, signals were greater than 3–6 dB. Linear and radial shear wave polarizations were also compared; a higher mode purity and signal intensity were obtained with the linear polarization.**

Index Terms— **Electromagnetic-acoustic transducer (EMAT), non-destructive evaluation (NDE), ultrasonic transducers.**

I. Introduction

ELECTROMAGNETIC acoustic transducers (EMATs) do not require direct contact with the specimen under test, and they outperform piezoelectric transducers in applications where couplant cannot be used, where there are unfavorable coating layers, or simply when noncontact transduction is required [1]–[4]. Moreover, EMATs are very versatile and various configurations exist that can be used to generate a whole range of ultrasonic waves, for example, longitudinal, shear, and different types of guided waves [5]–[13]. However, EMATs commonly operate at hundreds of volts, which tend to make the electronics bulky. Moreover, any devices operating at such voltage levels are unsuitable in environments where intrinsic safety certification is required, for example, in the oil and gas industry. Lower voltages can be used, but averaging is then required to increase the signal-to-noise ratio. In many applications, the properties of the specimen under test change while the test is being run, and this corrupts the results produced by averaging. Therefore, it is necessary to study how to increase the sensitivity of EMATs, so that they can be driven by compact, low voltage, and intrinsically safe electronics. The outcome of this paper can be applied to extending the battery life of battery-powered EMATs, which may lead to their use in long-term monitoring applications.

EMATs comprise a source for the bias magnetic field, such as that generated by permanent magnets, and a coil carrying alternating current [1], [2]. EMATs may rely on various transduction mechanisms, but this paper focuses on the Lorentz force as the dominant transduction mechanism in mild steel and ignores the influence of other mechanisms, such as magnetostriction; this assumption is sound based on [1] and [14]–[17]. When considering the Lorentz force as the dominant transduction mechanism, the bias magnetic field is of paramount importance, since the strength of the signal/wave increases in proportion to its magnitude on both transmission and reception.

According to recent publications, the strength of the bias magnetic field of EMATs can be increased by introducing other configurations more complex than a single magnet, which can be grouped under magnetic flux concentrators and repelling magnet configurations. In [18], a soft magnetic ribbon was placed between a permanent magnet and the coil. This acted as a flux concentrator for the bias magnetic field, which increased the flux density and the signal strength. In [19], a capped cone of ferromagnetic material was placed between a magnet and a ferromagnetic specimen. The capped cone concentrated the flux from the wider area of the magnet into a smaller area over the specimen, thereby increasing the flux density.

Two magnets arranged in a repelling configuration were employed in [20] and [21]. An increase in the magnetic flux density by a factor of almost two, compared with a single magnet, was achieved in the area between the repelling magnets. However, this improvement was constrained to small areas between the repelling magnets, and hence, its application was limited to small ultrasound apertures.

Configurations that combine flux concentration and repulsion mechanisms have already been proposed [22]–[24]. These basically consisted of a core of ferromagnetic (magnetically permeable) material surrounded by magnets with like poles facing the core. A strong magnetic field resulted inside the core, due to repulsion mechanisms between the magnets, which then escaped through the two remaining faces that are normal to the axis of symmetry. However, the dimensions of the core and the magnets that maximized the magnetic flux density within a given ultrasonic aperture and/or

Manuscript received December 1, 2015; accepted April 21, 2016. Date of publication April 27, 2016; date of current version August 1, 2016. The work of F. Cegla was supported by the Engineering and Physical Sciences Research Council under Grant EP/K033565/1.

The authors are with the Department of Mechanical Engineering, Imperial College London, London SW7 2AZ, U.K. (e-mail: j.isla13@imperial.ac.uk; f.cegla@imperial.ac.uk).

Digital Object Identifier 10.1109/TUFFC.2016.2558467

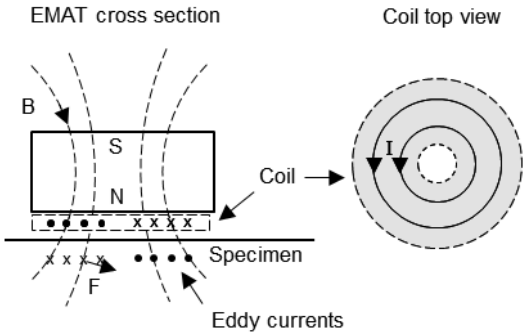

Fig. 1. Conventional EMAT comprising a single magnet and a pancake coil.

produce ultrasonic waves with high mode purity are still unknown.

Despite all these new configurations, there remains a need for more quantitative studies of the optimal configurations and dimensions of EMATs, such as that conducted in [25]. In [25], the effect of the ratio between the width of the magnet and coil area on the strength of the signal was investigated; the authors concluded that beyond a certain ratio, no major improvement in the signal strength was possible.

In this paper, we investigate several EMAT configurations that can be used for thickness gauging applications and compare their performance. Especial emphasis is given to that configuration that consists of a ferromagnetic core surrounded by repelling magnets. In addition, we studied the combined effect of the magnet configuration and the size of the ultrasonic aperture on the signal quality and intensity; the difference between linear and radial polarizations of shear wave EMATs was also addressed.

The organization of this paper is as follows. First, the basic theory behind the Lorentz force, as the dominant transduction mechanism of EMATs in mild steel, and the bias magnetic field will be introduced. Second, the configuration of the ferromagnetic core surrounded by the permanent magnets is described. The distribution of the magnetic flux density within this configuration and the specimen is studied by using finite-element (FE) simulations; the results are then compared with other configurations. Later, the effect of the size of the ultrasonic aperture on the signal strength and the mode purity of the ultrasonic waves in pulse-echo mode are investigated using the FE analysis. Following that the optimal dimensions of the core–magnet arrangement that maximizes the signals in the pulse-echo mode are investigated and compared with other configurations. Finally, the experimental results that show the superior performance of the optimized core–magnet arrangement are presented, and the conclusions are drawn.

II. Background

A. EMATs Based on the Lorentz Force

EMATs comprise a bias magnetic field and a coil that carries alternating current. One of the simplest commonly used configurations for EMATs is shown in Fig. 1. It consists of a single cylindrical permanent magnet placed on top of a pancake-like coil, such that radially polarized waves are generated [7].

EMATs exploit various transduction mechanisms (i.e., the Lorentz force, magnetostriction, and so on) depending on their configuration and the specimen properties [1], [2]. In mild steel, the main focus of this paper, the Lorentz force is assumed to be the predominant transduction mechanism for bulk waves; this assumption is sound based on [1] and [14]–[17]. It can be understood as follows. First, the coil of the EMAT induces eddy currents in a conductive specimen, whose path tends to mimic that of the coil. Then, these eddy currents with density $\mathbf{J_e}$ interact with the bias magnetic field, whose flux density is $\mathbf{B}$, and the resulting Lorentz force density on the charged particles (electrons) is given by

$$\boldsymbol{f} = \mathbf{J_e} \times \mathbf{B}. \tag{1}$$

The charged particles interact with the atomic structure of the material, which results in deformations that generate ultrasonic waves. In this paper, $\mathbf{B}$ refers to the bias magnetic field due to permanent magnets only, and any other contributions to the bias magnetic field, e.g., due to the eddy currents, are neglected.

The inverse effect also applies whereby an ultrasound wave forces the charged particles to move which, under a bias magnetic field, produce eddy currents under the surface of a conductive specimen with density

$$\mathbf{J_e'} = \sigma(\boldsymbol{v} \times \mathbf{B}) \tag{2}$$

where σ is the conductivity of the material and $\boldsymbol{v}$ is the velocity of the charged particles. These eddy currents are then inductively picked up by the coil of the EMAT. It should be noted that for an EMAT in pulse-echo configuration, the resulting signal is proportional to the square of the magnetic flux density $\mathbf{B}$, since it contributes twice on transmission and reception.

B. Formulation of the Bias Magnetic Field

The magnetic field $\mathbf{H}$ and the magnetic flux density $\mathbf{B}$ are related as follows:

$$\mathbf{B} = \mu_0(\mathbf{H} + \mathbf{M}) \tag{3}$$

where $\mathbf{M}$ is the magnetization vector. Magnetization can be expressed as

$$\mathbf{M} = \chi_m \mathbf{H} + \mathbf{M_0} \tag{4}$$

where $\mathbf{M_0}$ is the remanent magnetization and χ_m is the susceptibility of the material. A useful figure of merit for permanent magnets is its remanent flux density $\mathbf{B_r} = \mu_0 \mathbf{M_0}$. For static fields

$$\nabla \times \mathbf{H} = 0. \tag{5}$$

Thus, a scalar magnetic potential V_m can be defined as

$$\mathbf{H} = -\nabla V_m. \tag{6}$$

Substituting this back into (3) and using the fact that

$$\nabla \cdot \mathbf{B} = 0 \tag{7}$$

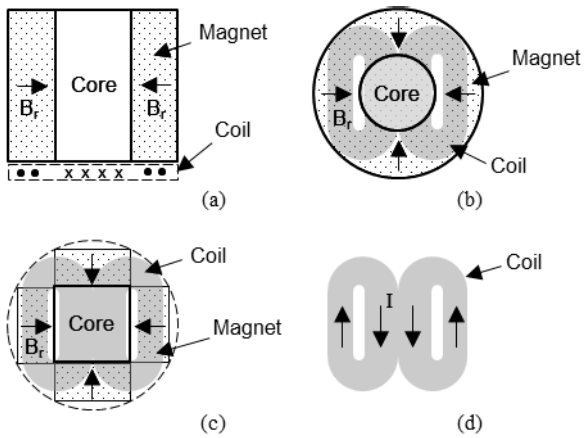

Fig. 2. Concentric arrangement of ferromagnetic core and permanent magnets with a butterfly coil. (a) Front view. (b) Top view of ideal configuration with cylindrical symmetry. (c) Top view of practical configuration with four magnets. (d) Direction of currents in the butterfly coil.

it is obtained

$$\nabla \cdot (-\mu \nabla V_m + \mathbf{B_r}) = 0 \tag{8}$$

where $\mu = \mu_0(\chi_m + 1)$. As discussed later in this paper, (8) can be solved using FE methods in order to obtain the distribution of $\mathbf{H}$ within a given volume, where a permanent magnet is present.

III. Concentric Arrangement of Ferromagnetic Core Surrounded by Permanent Magnets

A. Ideal Configuration and Practical Approximations

First, an ideal configuration is introduced to facilitate the FE simulations of the concentric arrangement of ferromagnetic core surrounded by permanent magnets. This ideal core–magnet configuration consists of a cylindrical magnet with its remanent flux density $\mathbf{B_r}$ oriented toward its center, where there is a permeable core [Fig. 2(a) and (b)]. This ideal approach is useful to simplify simulations due to its cylindrical symmetry. However, in practice, it is difficult to achieve such an orientation of $\mathbf{B_r}$ with only one magnet. By ideal configuration, we mean that it consists of an axisymmetric magnet whose remanent flux density is oriented toward the center, which is difficult to make in practice; the word ideal does not imply that the configuration itself is necessarily the optimal global solution to the problems or scenarios discussed in this paper. A good approximation can be obtained by several magnets, each having $\mathbf{B_r}$ oriented toward the ferromagnetic core. Fig. 2(c) shows an example using four magnets.

The rationale behind this core–magnet configuration can be understood as follows. Magnets with like poles facing each other produce an increase in the magnetic flux density in the space between them. An extra increase in the flux density is obtained by filling the gap between the magnets with permeable (ferromagnetic) material. It is interesting to mention that the permanent magnet arrangements with different magnet orientations in combination with permeable materials have been used in the past to significantly increase the magnetic flux density that can be generated by the magnet arrangement compared with a single magnet. These magnet arrangements can achieve 3 T [26], [27], 4 T [28], and 5 T [29]; however, they were developed for other purposes not related to EMATs.

Moreover, the use of the permeable core provides other advantages. For example, a flat distribution of the normal component of the flux density B_n can be obtained under the core for certain ranges of core and magnet dimensions. All of the cases discussed herein approximate this type of distribution for B_n. The core can also be made of nonconductive material, such as ferrite or laminated iron, so that the eddy currents, and the subsequent ultrasonic waves generated in the core, are practically eliminated.

B. Finite-Element Simulations of the Ideal Core–Magnet Configuration

The ideal cylindrical magnet was simulated in COMSOL Multiphysics 4.3b using the magnetic field, no current interface of the ac/dc module model library. This interface solves (8) by means of a Lagrange element formulation [30]. An axisymmetric (2-D) model was employed as a result of the magnet cylindrical symmetry.

The maximum length of the quadrilateral mesh elements (distance between the furthest nodes) was set to less than 0.1 mm under the core. Then, the length of the elements was increased progressively, so that the elements furthest from the core and the magnets reached a maximum length of 2 mm. A convergence test was conducted to confirm that the results did not change by more than 1% when using a denser mesh.

The space surrounding the structure was modeled as air. The height of the area simulated as air was three times the height of the structure, whereas the width of the area simulated as air was twice the width of the structure. Magnetic insulation boundaries were employed to enclose the region modeled as air; the axis of symmetry did not require a magnetic insulation boundary. The magnet had a height of 20 mm, a width (inner to outer radii difference) of 6.2 mm, and $\mathbf{B_r} = 1.42$ T [31]. $\mathbf{B_r}$ was oriented toward a soft iron core in the center, which had a radius of 5 mm. The magnet-core arrangement was positioned above a soft iron specimen, whose thickness was 10 mm. A 0.5-mm gap was left between the magnet-core arrangement and the specimen.

Due to the fact that the permeability of soft iron changes with the intensity of the field $\mathbf{H}$, a curve relating $\mathbf{B}$ versus $\mathbf{H}$ has to be used in the simulations to obtain the accurate results. This curve was obtained from the COMSOL library [30]. However, no significant changes were found in the distribution of B_n beneath the core when using other curves (e.g., for mild steel), because the strength of the field was very high in that region, and therefore, the different materials saturated easily.

C. Magnetic Flux Density Distribution of the Ideal Core–Magnet Configuration

Fig. 3(a) shows the results from the simulation. The absolute value of the flux density distribution is plotted using a gray scale in tesla, while the black lines represent the field lines. The field lines pass through the magnet toward the core, where their density increases as an effect of repulsion in the center of

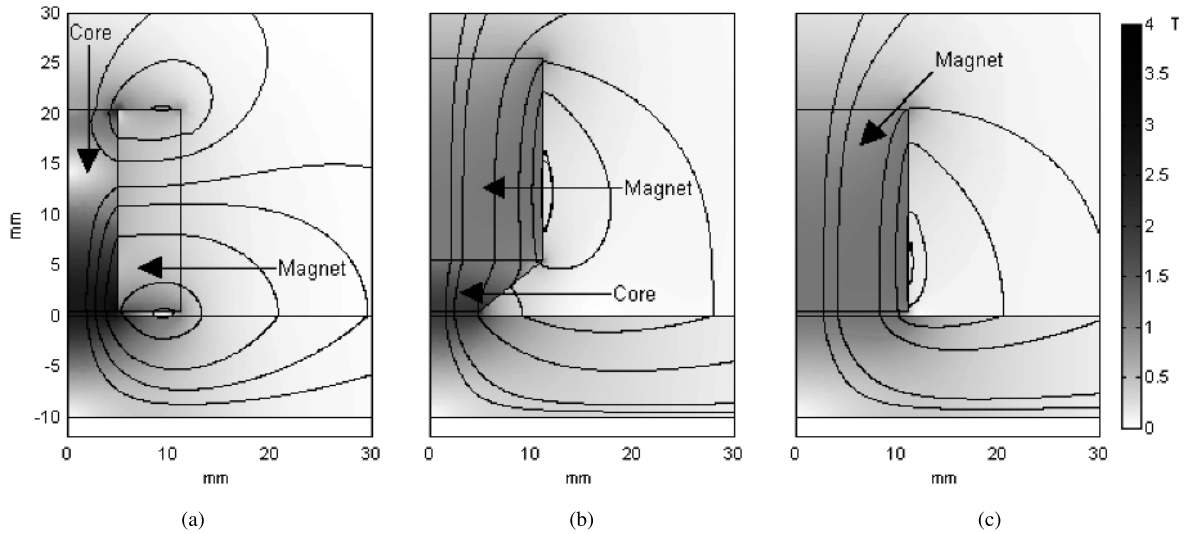

Fig. 3. Simulations of absolute magnetic flux density distribution of different EMAT configurations represented by a gray scale in tesla. Field lines are plotted with black lines. (a) Core–magnet arrangement. (b) Single magnet with a capped cone. (c) Single magnet.

the magnet. The lines then escape through the bottom and top sides of the core. Since the ferromagnetic specimen creates a higher permeability path compared with air, the flux density in the surface of the specimen beneath the core increases significantly.

At frequencies above a few tens of kilohertz, the eddy currents induced by the EMAT coil are concentrated within a few micrometers under the surface of a mild steel specimen due to the electromagnetic skin effect. That is where the transduction mechanism takes place, and hence, it is sufficient to study the normal and tangential components of the flux density (B_n and B_t, respectively) within that region in order to fully characterize the transduction mechanism. The flux density was found to vary little between 0 and 0.1 mm below the surface of the specimen; therefore, the simulations that employ resolutions higher than 0.1 mm will not add extra information to the results but will increase the computational burden.

The distributions of B_n and B_t at 0.1 mm below the surface of the specimen that correspond to Fig. 3(a) are shown in Fig. 4(a). It can be observed that B_n is fairly constant beneath the core, where it reaches the values above 2.5 T and then drops abruptly. When a butterfly coil is used, as shown in Fig. 2(a) and (b), this distribution of B_n is convenient to generate shear waves under the core that have single polarity and high mode purity.

The highest values of B_t appear under the magnet, where its mean value is roughly half of that achieved by B_n under the core. B_t is responsible for the generation of longitudinal waves; the longitudinal waves generated by this configuration have been found to be of much lower intensity than the shear waves.

D. Comparison With Other Configurations

The core–magnet arrangement is now compared with other EMAT configurations. A cylindrical magnet is shown in Fig. 3(c), and only half of the cross section of the magnet is shown due to its symmetry. To give a fair comparison, the volume of this single magnet is equal to that of the core and the magnet of Fig. 3(a) combined. Its $\mathbf{B_r} = 1.42$ T is also the same but oriented toward the specimen.

Fig. 4(c) shows B_n and B_t distributions that correspond to the single magnet case at 0.1 mm below the surface of the specimen. The highest values of B_n are reached beneath the magnet, and these do not increase far above 1.2 T regardless of the size of the magnet. The maximum values of B_t occur at the edge of the magnet, and they are of equivalent magnitude to those of B_n.

It is important to highlight that the use of a single magnet to produce single polarization shear waves is impractical, because the coil tracks must have a single orientation under the magnet and a return path elsewhere. This return path adds extra volume to the EMAT. A pancake-like coil, as shown in Fig. 1, is a volume efficient solution for a single magnet, but radially polarized waves are generated instead. The disadvantages of the radially polarized waves will be addressed later on.

Fig. 3(b) shows the same single magnet but on top of a capped cone of ferromagnetic material; this configuration was reported in [19]. The radius of the bottom face of the capped cone is 5 mm—this is equal to the radius of the core–magnet arrangements of Fig. 3(a) to give a fair comparison—whereas the height of the capped cone is 5 mm. Different values were explored through simulations revealing that when the cone height was either increased or decreased by a few millimeters, no significant differences were found in the results.

In Fig. 3(b), the field lines from the magnet go through the capped cone, where the flux density increases as the transversal area of the cone is reduced. Most of the lines do not abandon the cone before entering the specimen, because a high permeability path exists between the cone and the specimen. However, when the gap between the bottom of the cone and the specimen increases, a high reluctance region is introduced and a significant part of the field leaves the cone without reaching the specimen. This makes this particular configuration very

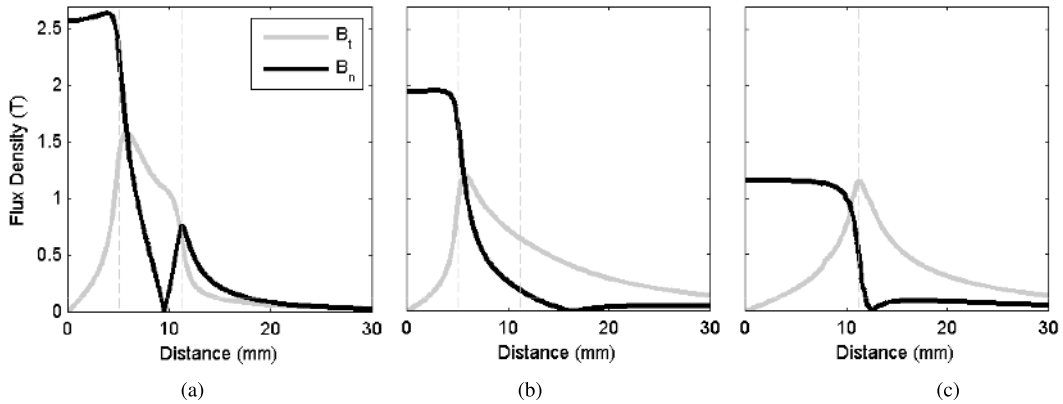

Fig. 4. Normal B_n (black line) and tangential B_t (gray line) flux density distribution simulations at 0.1 mm under the specimen surface for different EMAT configurations. (a) and (b) Vertical dashed lines on the left indicate the radius of the core/capped cone face closest to the specimen, whereas the ones on the right indicate the outer diameter of the EMAT. (c) Vertical dashed line indicates the outer diameter of the EMAT.

sensitive to the EMAT liftoff (i.e., the gap between the bottom of the cone and the specimen).

Fig. 4(b) shows the corresponding B_n and B_t distributions at 0.1 mm below the surface of the specimen. It can be observed that the behavior of the field within the footprint of the cone is similar to that of Fig. 4(a) but with smaller values.

Overall, the use of any conical core has a detrimental effect on the intensity of the field in the specimen, especially when the liftoff increases. This is one problem found in [22] and [23], where a core–magnet arrangement was proposed similar to that of Fig. 3(a), but whose core bottom section had a conical shape. As a result, the magnets surrounding the core had to be separated from the specimen. The authors have observed that in the case of a core–magnet arrangement, the greatest flux densities within the specimen are achieved when the bottom face of the core is aligned with that of the surrounding magnets, as shown in Fig. 2(a) and (b).

IV. Influence of the Ultrasound Aperture Area and Polarization on Signal Strength and Quality

When extracting the time of flights of signals for thickness gauging applications, the signals received should have very low distortion and the greatest amplitudes possible in order to avoid errors. Therefore, it is important to understand how the aperture area and the polarization affect the received signals. To do so, FE simulations using the COMSOL Multiphysics 4.3b Solid Mechanics module were carried out.

A. Finite-Element Simulations Setup

In a first stage, a circular aperture with radial polarization, as shown in Fig. 1, was investigated. An axisymmetric (2-D) model sufficed, because cylindrical symmetry could be exploited. In the second stage, the same aperture area was studied but using linear polarization, as shown in Fig. 2, and a 3-D model due to the lack of cylindrical symmetry. In both stages, the general procedure was: 1) to apply a boundary load to the surface of a mild steel specimen within the aperture area; 2) to simulate the propagation of the ultrasonic waves; and 3) to record the velocity of the reflected ultrasonic waves on the same surface where the boundary load was applied.

The axisymmetric model comprised a rectangular region simulated as mild steel (the density of 7850 kg/m^3, the Young modulus of 205 GPa, and the Poisson ratio of 0.28). The thickness of this region was set to 5, 10, and 15 mm in a parametric study. The width of this region matched the area of the aperture and was varied from 2.5 to 10 mm in 2.5-mm intervals. One side of the rectangle was set as the axis of symmetry, whereas the other side was coupled to multiple absorbing regions, as described in [32]—this is to reduce wave reflections from this side. The outer boundary of the absorbing region parallel to the axis of symmetry was fixed to prevent the displacement of the whole structure when the load was applied; the remaining boundaries were free to move.

The mesh employed quadrilateral elements with the maximum length (distance from the furthest nodes) of 0.27 mm, and this is roughly 1/6th the shear wavelength in mild steel at 2 MHz (1.6 mm). A time domain simulation was conducted using the time steps with a period equivalent to a sampling frequency of 32 MHz. The excitation signal was a three-cycle Hanning tone-burst centered at 2 MHz. The excitation was applied as a force (boundary load) tangential to the surface. The force density on the surface was in the order of a few nN/m^2—the exact values were not relevant, since only relative values were used in the analysis of the results. Once every parameter was specified, a convergence test was conducted to confirm that neither a denser mesh nor a higher sampling frequency improved the results by more than 2%.

The results from the simulations are shown in Fig. 5(a)–(c), and these are the sum of the radial component of the velocity of the reflected signals at the excitation nodes. The signals are normalized to the maximum value of the first echo to establish a qualitative comparison between the signals. Note that some of the excitation bursts were clipped because of this. The aperture diameter and the specimen thickness are specified in each case.

The 3-D model used to investigate the linearly polarized aperture was obtained by revolving the 2-D model, a quarter of a circumference around its axis of symmetry. Then, symmetric

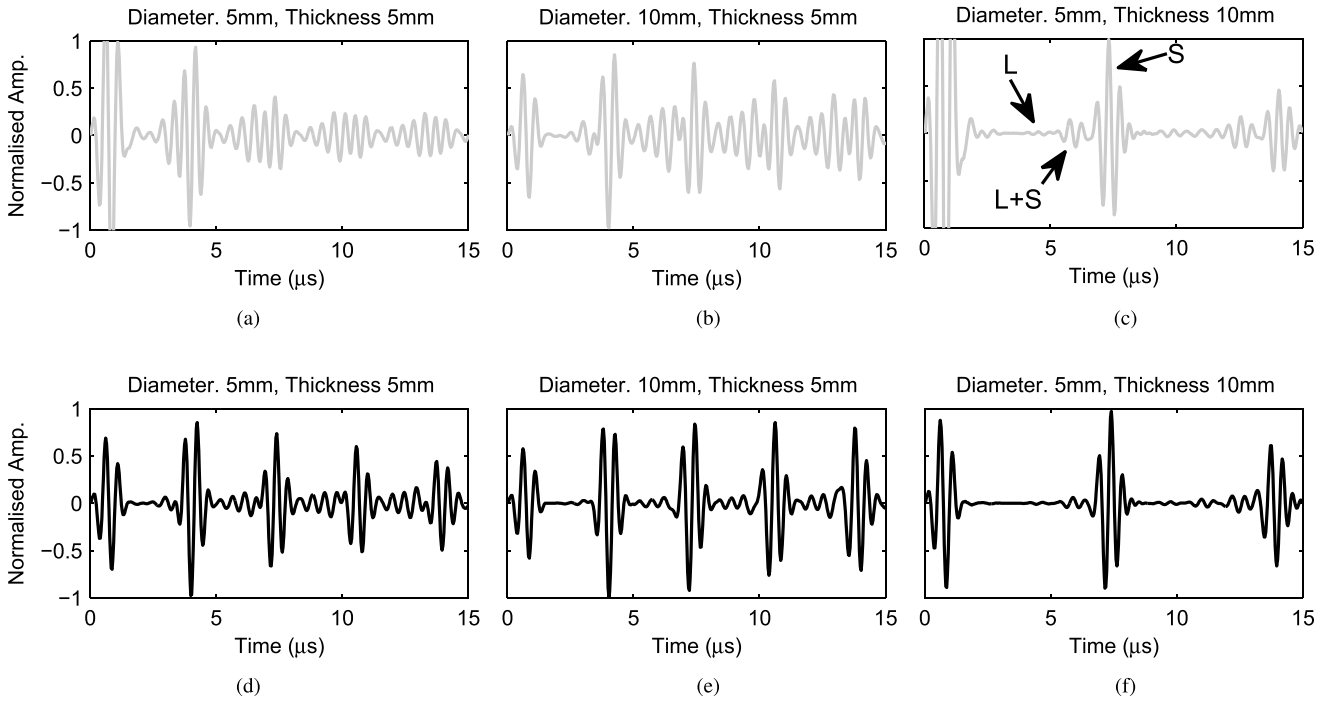

Fig. 5. Signals from FE simulations. (a)–(c) Radially polarized apertures (gray traces). (d)–(f) Linearly polarized apertures (black traces). All of the signals are normalized to the maximum value of the first echo.

and antisymmetric boundaries were used appropriately with respect to the orientation of the load, which was applied in a direction parallel to the symmetric boundary. The remaining settings were the same used in the 2-D simulation, except for the use of tetrahedral elements in the mesh. To establish a fair comparison, the same aperture diameters and the specimen thicknesses of the 2-D model were simulated. The tangential component to the aperture area of the velocity of the reflected signals (also parallel to the symmetric boundary) is shown in Fig. 5(d)–(f).

B. Signal Distortion in Pulse-Echo Mode

By looking at the signals in Fig. 5, three main observations can be drawn: 1) radially polarized apertures produce higher distortion; 2) distortion decreases when the aperture area increases; and 3) distortion decreases when the thickness increases. We analyzed the wave fields in each particular case and determined that the distortion of the signals was caused by the direct generation of the longitudinal mode and by mode conversion upon reflections. In Fig. 5(c), the echoes due to the longitudinal and shear modes are labeled as L and S, respectively, whereas the mode converted is labeled as $L+S$.

In the case of the radially polarized shear aperture, the longitudinal mode is generated in its center and edge. This is because the discontinuity of the applied forces in those regions causes compression and rarefaction, creating a point source in the center of the aperture and a curved line source on the edge. Fig. 6(a) shows an axisymmetric view of a radially polarized aperture, where the location of the longitudinal apertures can be appreciated. The reflection paths of the pure modes, shear, and longitudinal are also shown. Fig. 6(b) shows an example of mode conversion from longitudinal to shear ($L+S$); other combinations are omitted for simplicity.

On the other hand, when the aperture is linearly polarized, the longitudinal mode is mainly produced on that section of the edge of the aperture perpendicular to the applied force. This explains why the linearly polarized aperture produces less distortion (or a weaker longitudinal mode) than the radial one.

Distortion decreases when the aperture area increases, because the proportion of the area that generates the shear mode increases with respect to the length of the line (and point) sources that generate the longitudinal mode. Finally, distortion decreases when the thickness increases, because the line sources are more affected by beam spreading than the larger areas that generate the shear mode.

C. Signal Amplitude in Pulse-Echo Mode

The following inequation sets an upper bound for the intensity of the reflected signals S given a transducer area A:

$$S \leq \iint G_t G_r \, dA \tag{9}$$

where dA is the infinitesimal area of the aperture, while G_t and G_r are the transduction gains on transmission and reception, respectively. This inequation is necessary to account for the beam spreading effect.

Assuming that the Lorentz force is the main transduction mechanism and that eddy currents follow a uniform distribution, (9) can be rewritten, such that the transduction gains G_t and G_r are expressed as a function of the magnetic flux density B. This is because in the pulse-echo mode, the magnetic flux density distribution and the aperture area

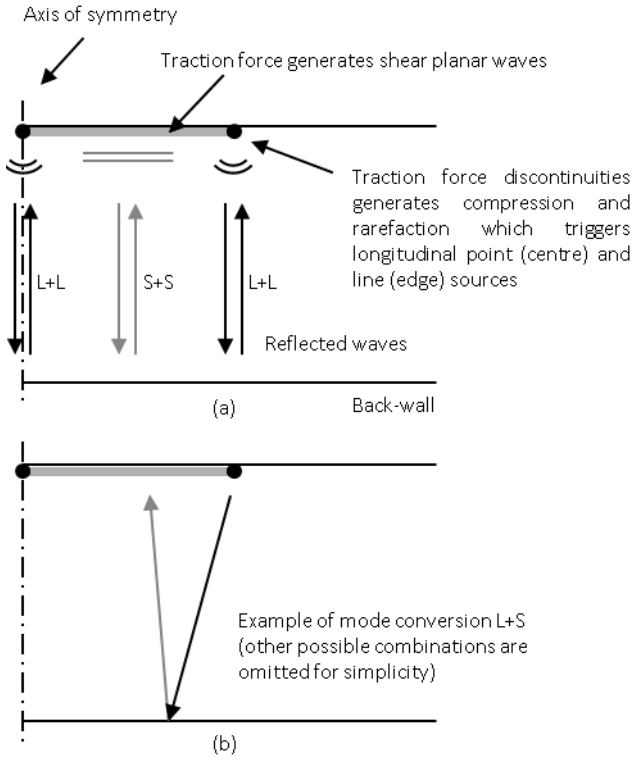

Fig. 6. Longitudinal mode generation in radially polarized shear aperture (axisymmetric view). (a) Traction force discontinuities generate compression and rarefaction, which trigger longitudinal point (center) and line (edge) sources. (b) Example of mode conversion $L + S$; other possible combinations are omitted for simplicity.

are the same on reception and transmission. Provided the coil shape is also the same on reception and transmission, it can be written as

$$S \leq \alpha' \iint B^2 dA \tag{10}$$

where α' is a constant.

Fig. 7 shows the amplitude of the first echo of the simulated signals for different aperture diameters and specimen thicknesses. The black markers stand for the linearly polarized apertures, whereas the gray markers represent the radially polarized apertures. For simplicity, and without loss of generality, G_t and G_r can be assumed constant. Then, they can be combined into a single constant α. The black continuous curve in Fig. 7 was obtained by evaluating the upper bound of (9) and choosing α, so that the curve matches the marker with the greatest value in Fig. 7.

It can be observed in Fig. 7 that the markers that correspond to aperture diameters larger than 10 mm and specimen thicknesses smaller than 15 mm lie very close to the solid black curve. In other words, the amplitude S of each of the reflected echoes that correspond to these markers is very close to their maximum value, which is the right-hand side of (9). This is because in these cases, the beam spreading is negligible.

In general, the linearly polarized aperture (black markers) achieves greater echo amplitudes than the radially polarized aperture (gray markers) for each aperture diameter and specimen thickness. The difference in echo amplitudes between the

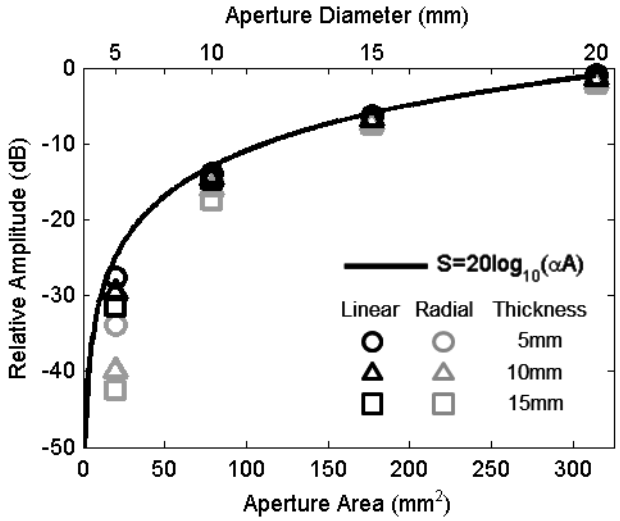

Fig. 7. Maximum amplitude of the first echoes of the simulated signals for different aperture diameters, polarizations, and specimen thicknesses. The black continuous curve was obtained by evaluating the equality in (9) and choosing α so that the curve matches the marker with the greatest value.

linear and radial apertures increases, as the aperture diameter decreases and the specimen thickness increases. Note that for 10-mm apertures and thicknesses greater than 15 mm, this difference is greater than 3 dB.

V. Optimal Dimensions of the Core–Magnet Arrangement

In this section, the optimal dimensions of the core–magnet arrangement are explored. The optimization objective is to maximize (10). Results from the core–magnet arrangement are compared with those of other configurations, especially the single magnet EMAT. At the end of this section, the effect of the specimen thickness on the results is investigated.

A. Effect of Height, Core, and Overall Diameter

The ideal cylindrical core–magnet arrangement of Fig. 2(a) was simulated in COMSOL Multiphysics 4.3b employing cylindrical symmetry. A parametric study was conducted, where the height of the arrangement was set to 10, 20, and 40 mm; the diameter of the core was set to 10 and 20 mm; and the width of the magnet (inner to outer radii difference) was changed to obtain EMAT overall diameters between 15 and 50 mm. The remanent flux density was set to $\mathbf{B_r} = 1.42$ T (N52 [31]) and oriented toward a soft iron core in the center. Both magnet and core had a liftoff of 0.5 mm from a soft iron specimen that had a thickness of 10 mm. As in Section III-B, a curve relating $\mathbf{B}$ versus $\mathbf{H}$ was employed for soft iron, which was obtained from the COMSOL library [30].

The value of B_n under the surface of the specimen was squared and integrated over the area of the core to compute the expected signal strength based on (10)—the results are shown in Fig. 8(a). Continuous gray and black curves represent 5- and 10-mm-diameter cores, respectively, whereas the dashed gray curves correspond to 20-mm-diameter cores. Different EMAT heights were employed (10, 20, and 40 mm) for each core diameter represented by each family of curves. The position

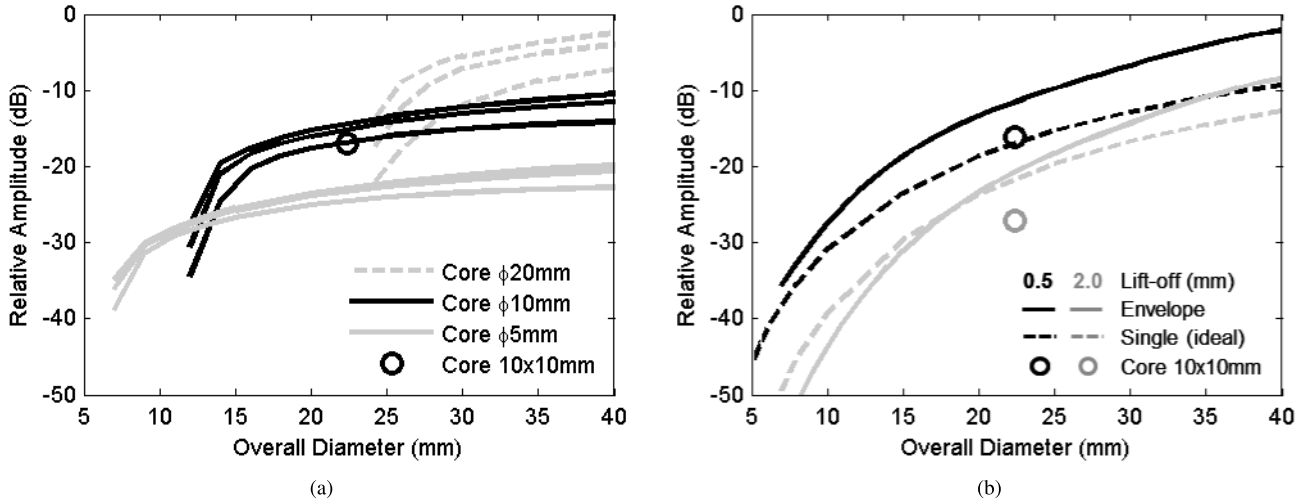

Fig. 8. Simulations of the signal strength according to (10) versus EMAT overall diameter for the core–magnet arrangement. (a) Continuous gray and black curves represent 5- and 10-mm-diameter cores, respectively, whereas the dashed gray curves correspond to 20-mm-diameter cores; for each diameter, there are different EMAT heights (10, 20, and 40 mm) that correspond to each family of curves from bottom to top. (b) Black and gray curves represent the liftoffs of 0.5 and 2 mm; the overall height in each case is 20 mm; the continuous curves represent the envelope of the resulting family of curves for different core diameters of the core–magnet arrangement (fourth-order interpolation for core diameters between 5 and 25 mm in 5-mm intervals), whereas the dashed curves correspond to the single magnet. Curves were arbitrarily normalized. The circle markers correspond to a 3-D model of an EMAT with a height of 20 mm, a core with a square base of 10×10 mm^2, and the magnets with the rectangular bases of 5×10 mm^2, as shown in Fig. 2(c).

of the curves in the family is positively correlated with the height of the EMAT, such that the smallest heights correspond to the curves with the smaller values. Curves were arbitrarily normalized since only the relative values are of interest.

Overall, the improvement when increasing the height of the core–magnet arrangement from 10 to 20 mm is nearly 3 dB; from 20 mm onward, the signal increase is not greater than 2 dB. In addition, an increase in the width of the magnet (inner to outer radii difference) produces a steep increase in the signal when the width is less than the radius of the core. When the magnet width is greater than the radius of the core, the signal still increases but at a lower rate. Then, it can be inferred that there is a core diameter that maximizes the signal strength per overall unit area of the EMAT.

To investigate the effect of liftoff on the signal intensity, the calculations were repeated for core diameters between 5 and 25 mm in the intervals of 5 mm using an overall height of 20 mm and the liftoffs of 0.5 and 2 mm. Fig. 8(b) shows the envelope of the resulting family of curves using a fourth-order interpolation—the continuous black and gray curves correspond to 0.5 and 2 mm, respectively. For example, it can be observed that when the liftoff is 0.5 mm, the optimal overall diameter for a 10-mm-diameter core is roughly 17 mm, whereas for a 20-mm-diameter core is roughly 30 mm [see corresponding curves in Fig. 8(a)]. Then, the optimal ratio between the core and the overall diameter was found to be roughly 2:3 for these cases.

If the liftoff increases to 2 mm, the signal drops. The difference between the curves of 0.5- and 2-mm liftoffs is 5 and 10 dB for lower and higher overall diameters, respectively, so the larger the core, the smaller the signal drop with liftoff. Moreover, this drop also implies that the optimal ratio between the core and the overall diameter is roughly 1:2 for 2-mm liftoff.

Finally, a core–magnet arrangement with a core of square base of 10×10 mm^2 and magnets with the rectangular bases of 5×10 mm^2, as shown in Fig. 2(c), was simulated using a 3-D model. This type of core–magnet arrangement is easier to build in practice. The height of the core–magnet arrangement was set to 20 mm, and the rest of the parameters of the simulation were kept the same. The relative amplitude of the signal and the outer diameter of the EMAT for this configuration are shown in Fig. 8 with a circle marker. The results show that there is roughly 2.5-dB signal loss when using this configuration compared with the ideal cylindrical case irrespective of the liftoff. This can be explained by the loss of magnetic material in the core–magnet arrangement volume compared with a fully axisymmetric magnet encircling the core. For this overall diameter and height, there could be a different combination of core–magnet dimensions that optimize the signal amplitude, but this was not further explored, because it is computationally expensive.

B. Comparison With Other Configurations

Using (10), the performance of the core–magnet arrangement was compared with those of a single magnet as in the EMAT of Fig. 3(c) and a single magnet with a capped cone beneath it [Fig. 3(b)]. The distribution of B_n, required to calculate the expected signal strength in (10), was obtained through the simulations, as in Sections III-C and V-A.

To give an unbiased comparison, the diameter of the bottom base of the capped cone was set to 10 and 20 mm to match the diameter of the core of the core–magnet arrangement of Fig. 8(b); the height of the capped cone was set to 5 mm. For each configuration, the magnet height was set to 20 mm and the width/diameter was changed, so that the resulting diameter of the EMATs was between 5 and 50 mm. All the

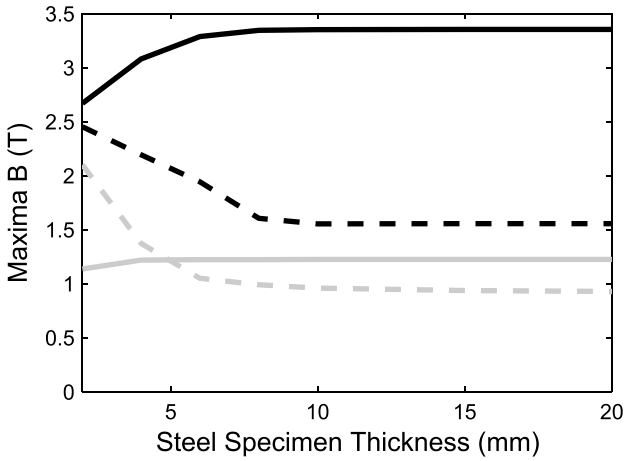

Fig. 9. Simulation of the maxima of B_n (continuous line) and B_t (dashed line) at 0.1 mm beneath the specimen surface versus specimen thickness. The black lines correspond to the core–magnet arrangement, while the gray ones correspond to the single magnet.

remaining parameters of the simulations were the same as those used to obtain the results of Figs. 3 and 8.

The strength of the signal produced by the single magnet according to (10) was shown in Fig. 8(b) using the dashed lines (black and gray for 0.5- and 2-mm liftoffs, respectively). It can be observed that when the liftoff is 0.5 mm, the optimal core–magnet arrangement outperforms the single magnet by more than 3 dB when the overall diameter is greater than 20 mm.

In practice, the difference between the optimal core–magnet arrangement and the single magnet should be greater, because the single magnet EMAT is assumed to have a linearly polarized aperture. Such an aperture requires an extra space for the return path of the coil, which increases the EMAT overall diameter. Moreover, if pancake-like coils were to be used, the resulting wave would be radially polarized, which also produces weaker (and more distorted) signals, as discussed in Section IV.

The gray traces in Fig. 8(b) show how the signal intensity is affected when the liftoff of the EMAT increases to 2 mm. Compared with the core–magnet arrangement, the single magnet EMAT is less affected by liftoff increase especially for smaller aperture diameter.

The single magnet with a capped cone beneath was found to produce the weakest signals among all the configurations for each case. Different heights for the capped cone were explored without significant changes in the results. These simulation results are not shown for the sake of brevity.

C. Influence of the Specimen Thickness

In the following simulations, a single magnet (40-mm height and 20-mm diameter) and a core–magnet arrangement (10-mm-diameter-core, 50-mm outer diameter, and 40-mm height) both with a liftoff of 1 mm from a ferromagnetic specimen were employed. The thickness of the ferromagnetic specimen was varied between 2 and 25 mm. The maximum of the normal flux density B_n and tangential flux density B_t was computed for every case at 0.1 mm below the surface; the results are shown in Fig. 9.

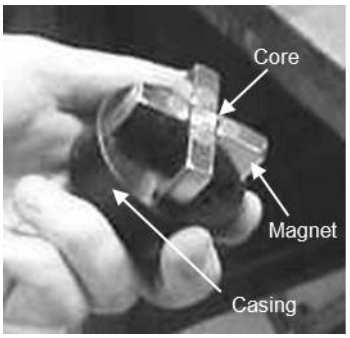

Fig. 10. Core–magnet arrangement used in the experiments. A black polymer casing holds the magnets and the core. The height of the magnets and the core is 40 mm. The core base is 10×10 mm^2, and the magnet bases are 10×20 mm^2.

Regardless of the EMAT configuration and its dimensions, there is a minimum thickness, whose exact value depends upon the EMAT configuration and dimensions, in Fig. 9, it is roughly 7 mm, where B_n starts decreasing and B_t increasing. The reason is that for thin specimens, the field is trapped inside the saturated specimen, due to its permeability being higher than air, and consequently, the field is forced to bend immediately when entering the specimen in order to reach the opposite pole.

VI. Experiments

The goal of the experiments was to assess the accuracy of (10) and the simulations, so that the results shown in Fig. 8 could be validated. To do so, the magnetic field produced by a single magnet and the core–magnet arrangement was measured and compared with the simulations in Section VI-A. In addition, the signals produced by different magnet configurations on the same coil were investigated and then compared with the simulation results in Section VI-B.

A. Magnetic Field Measurements

A photograph of the core–magnet arrangement that was constructed is shown in Fig. 10. It consists of four cuboid magnets with dimensions $40 \times 10 \times 20$ mm^3, which were made out of Neodymium N42 with remanent flux density $\mathbf{B_r} = 1.32$ T (Part No. F401020-1, Magnet Expert Ltd., U.K.). Like poles of each magnet were oriented toward a ferromagnetic mild steel core, which had dimensions $40 \times 10 \times 10$ mm^3. The magnets and the core were encased in a cylindrical container made out of polymer.

Two single magnets were built by stacking four 10-mm-thick magnets to mimic 40-mm-height magnets. Two different sets using 10- and 20-mm diameters were built (Part No. F674-4 and F646-1, respectively, Magnet Expert Ltd., U.K.).

The magnetic flux density from the stacked magnets and the core–magnet arrangement were measured using a Gaussmeter (GM08, Hirst Magnetic Instruments Ltd., U.K.) and a transverse Hall probe (TP002, Hirst Magnetic Instruments Ltd., U.K.). Both a single magnet and the core–magnet arrangement were placed on top of a mild steel block ($200 \times 200 \times 50$ mm^3) using a plastic layer that had

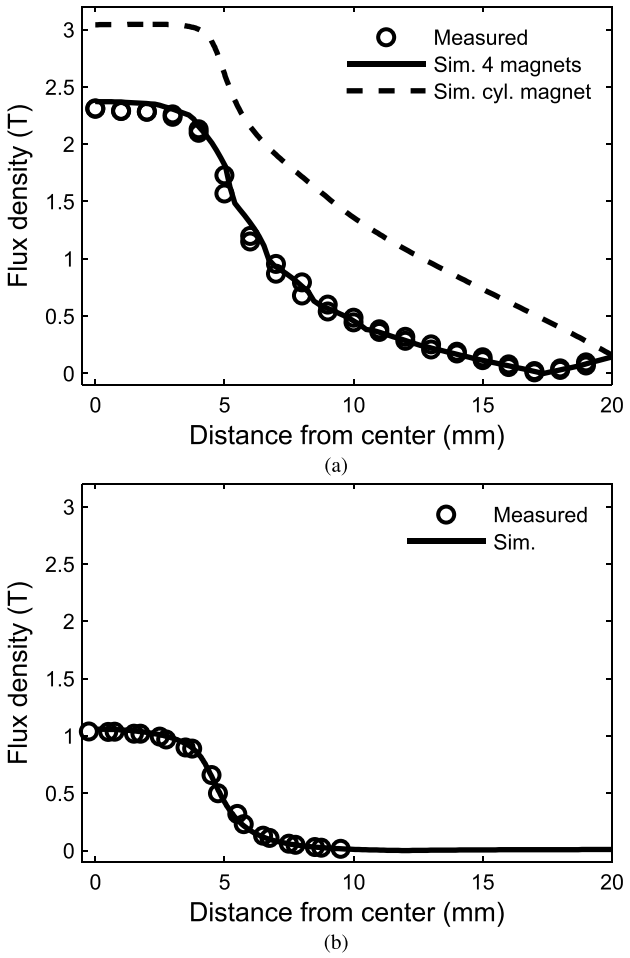

Fig. 11. Magnetic flux density of a core–magnet arrangement and a cylindrical magnet. (a) Core–magnet arrangement consisting of four cuboid magnets with dimensions $40 \times 10 \times 20$ mm^3 and a mild steel core with dimensions $40 \times 10 \times 10$ mm^3; the field is measured from the center of the core and beneath one of the magnets. The dashed curve in (a) corresponds to a simulation of the core–magnet arrangement using cylindrical symmetry. (b) Cylindrical magnet with a diameter of 10 mm and a height of 40 mm. All the magnets are made out of Neodymium N42 with remanent flux density $\mathbf{B_r} = 1.32$ T. The circle markers correspond to the measured fields and the solid black lines to the simulations.

a thickness of 1 mm. The plastic layer had a slot, along which the Hall probe was slid in 0.5-mm steps from the center of the magnets or core. In the case of the core–magnet arrangement, the slot was aligned with one of the magnets and the center of the core.

Fig. 11(a) and (b) shows the measured magnetic flux density of the core–magnet arrangement and single magnet using circle markers, respectively. Two sets of measurements are shown for each case to provide an overview of the variability of the results. The solid lines in Fig. 11(a) and (b) correspond to simulations; the procedures to conduct these simulations were the same as those described in Section III for cylindrical and 3-D models. Overall, there is good agreement between simulations and measurements.

As a comparison point, a simulation of the core–magnet arrangement using cylindrical symmetry is shown in Fig. 11(a) with a dashed curve. This cylindrical configuration corresponds to a 10-mm-diameter core with 50-mm overall diameter. It produces a greater flux density, but is also more difficult to build in practice.

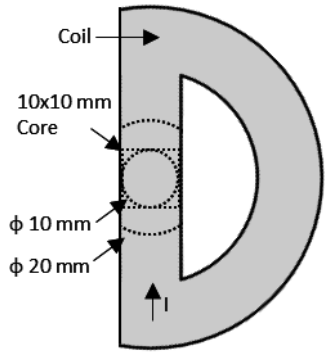

Fig. 12. D-shape coil with 22 turns of enameled wire used in the experiments. In different experiments, the circular magnets of diameter 10 and 20 mm and the 10×10 mm^2 square section core were centered in the straight region of the D-coil as shown.

B. Signals From Single Magnet and Core–Magnet Arrangement Configurations

A D-shape coil was built, as shown in Fig. 12, by winding 22 turns of enameled wire with a diameter of 0.4 mm, so that the resulting width of the coil in its straight section was 10 mm. One core–magnet arrangement and two single magnets of diameters 10 and 20 mm were placed over the straight section of the D-coil at a time, as shown in Fig. 12. The same coil was used in each case to avoid different coil shapes/impedances affecting the results. A D-shape coil was employed, because it is easy to build and produces linearly polarize waves under its straight section.

The coil was connected to a pulse-echo system (WaveMaker-Duet—custom made for the NDE Group of Imperial College London), which comprises a driver with an output trigger signal and a receive preamplifier. The driver of the system was configured to excite the coil with a three cycle Hann tone-burst at 2 MHz with a maximum peak-to-peak current of 200 mA. The shape and intensity of the tone-burst was monitored throughout the experiments with a noninvasive current sensor (Bergoz CT-B0.1-B) connected to an oscilloscope (LeCroy WaveRunner 44Xi).

The receive preamplifier of the system was set to amplify the signal by 60 dB; the receive signal amplitude was in the millivolt range. The output of the receive preamplifier and the output trigger signal from the driver were also connected to the oscilloscope. For each EMAT, the acquired signals were synchronized with the trigger signal from the driver and then averaged 4000 times in the oscilloscope, so that the electrical random noise was attenuated far below the coherent noise present. Any remaining coherent noise could be due to the generation and reverberation of ultrasonic waves inside the magnets and/or the electronics.

Fig. 13 shows the signals from the measurements on a 50-mm-thick specimen (with parallel flat surfaces and free from defects) corresponding to the three cases tested. Since the purpose of the experiments was to compare

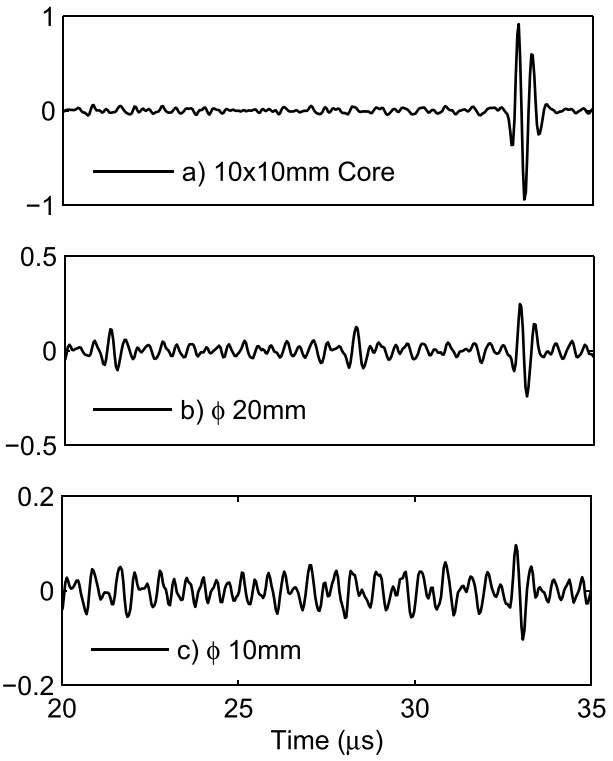

Fig. 13. Signals from pulse-echo measurements on a 50-mm-thick mild steel specimen. (a) Core–magnet arrangement. (b) 20-mm-diameter single magnet. (c) 10-mm-diameter single magnet. Signals are normalized to the maximum value and plotted with different scales in each case.

different configurations, and the absolute voltage measured is dependent on the instrumentation used, the results were arbitrarily normalized—note that the amplitude scale of Fig. 13(a)–(c) is different in each case.

The reflected echoes from the back wall of the specimen can be observed at the right end of the plots at $\sim$33 μs. As expected, the core–magnet arrangement produced the strongest signals followed by the 20-mm-diameter single magnet. The coherent noise floor is the same in each case and is shown in Fig. 13(c) to be $\sim\pm 0.05$; the noise amplitude corresponds to roughly 5% of the signal produced by the core–magnet arrangement.

In Fig. 13(b), two echoes were identified at $\sim$21 and 28 μs (6.4-μs difference), which corresponds to the thickness of the 10-mm-height magnets that were stacked to mimic the single magnet EMAT. The echoes are likely to be reverberations inside the magnets, which have also been observed previously [33]. Similar echoes are likely to be present in Fig. 13(c), but they could not be identified due to the level of the noise.

Finally, the relative signal amplitudes of the three EMATs were estimated using (10), where the magnetic flux density distribution beneath the surface of the specimen was obtained from simulations; simulation details are discussed in Section III for cylindrical and 3-D models. The estimated liftoff for each configuration was 0.5 mm. Simulated and experimental results are compared in Fig. 14. The results are normalized to the values corresponding to that of the 20-mm-diameter magnet to simplify the analysis of the results.

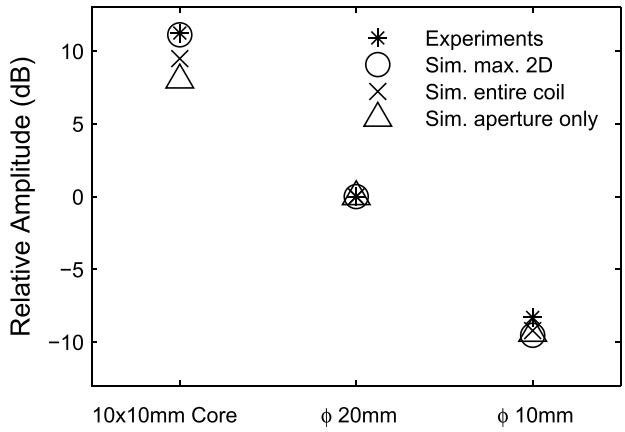

Fig. 14. Relative signal amplitude for the single magnets of 10- and 20-mm diameters and the core–magnet arrangement. Results are normalized with respect to the 20-mm-diameter magnet.

The asterisk markers show the measured relative signal amplitude for each configuration. The cross markers correspond to 3-D simulations considering the contribution of the field beyond the core/magnet, i.e., considering the nearby coil sections, while the triangle markers only consider the field beneath the intersection of the coil and the core or cylindrical magnets, i.e., the active aperture. The circle markers correspond to the maximum flux density from simulations using cylindrical symmetry over the core active aperture area. In the case of the core–magnet arrangement, this corresponds to a core diameter of 10 mm and a overall diameter of 50 mm.

In general, there is good agreement between the measured and simulated results, which confirms the validity of (10). In every case, the contribution of the field outside the active aperture is relatively small, less than 1.5 dB, with the greater difference corresponding to the core–magnet arrangement. It can be concluded that when the diameter of the ultrasonic aperture is 10 mm, the core–magnet arrangement produces signals roughly 20 dB greater than that of the single magnet.

In the core–magnet arrangement case, the experimentally measured values are roughly 3 dB higher than the simulated results (using the 20-mm-diameter magnet as the reference point). A combination of several factors could have caused this difference, for example, dimensional differences, the signals from the 10- and 20-mm-diameter magnets being overestimated due to the coherent noise of the amplifier or the influence of other transduction mechanisms, such as magnetostriction.

VII. Conclusion

This paper presented an in-depth analysis of the bias magnetic field strength and resulting signal amplitude of different magnet configurations for shear wave EMATs on mild steel. The Lorentz force was assumed to be the dominant transduction mechanism neglecting any other mechanisms, such as magnetostriction; experimental results showed no contradiction with this assumption. A particular core–magnet arrangement was found to produce pulse-echo signals, from a flat back wall, greater than 3–6 dB compared with a single magnet when EMATs of the same overall volume were compared—the

exact difference depends on the EMAT geometry in each particular case. The configuration that consists of a single magnet with a ferromagnetic capped cone beneath it was found to perform worse than the single magnet of equivalent overall volume. The core–magnet arrangement also produces signals 20 dB greater than a single magnet when the aperture diameter is 10 mm. This is due to the high magnetic flux density generated beneath the core in the center of the EMAT, which can exceed 3 T.

The enhanced performance of the presented core–magnet arrangement relies on increasing the magnetic flux density within a given area of interest by exploiting two mechanisms: 1) repulsion between magnets and 2) the flux guide formed by both the ferromagnetic core between the repelling magnets and the ferromagnetic specimen itself. The effective use of these mechanisms could be in principle generalized to others EMAT configurations.

It was also found that for each overall diameter of the core–magnet arrangement, there is a core diameter that maximizes the signal. When the height of the core–magnet arrangement is 20 mm and the liftoff is 0.5 mm, the optimal ratio between the core and overall diameter is roughly 2:3 for core diameters between 10 and 25 mm. This optimal ratio decreases to roughly 1:2 when the liftoff increases to 2 mm. It should be highlighted that these ratios only apply to their respective configurations when placed on mild steel specimens.

Moreover, another finding was that linearly polarized apertures, as in the core–magnet arrangement with a butterfly or D-shape coil, produce pulse-echo signals with greater amplitude and less distortion than the radially polarized apertures, as in the case of a single magnet with a pancake-like coil. Distortion is caused by the generation of the longitudinal mode; its effect decreases when either the area of the aperture or the thickness of the specimen increases.

In general, the core–magnet arrangement produces high purity shear waves, but this is limited by the thickness of the ferromagnetic sample. The tangential component of the magnetic flux density is responsible for the intensity of longitudinal mode, which causes distortion, and it was found to increase steeply for mild steel samples with thickness below 7 mm.

VIII. Supporting Information and Data Access

In order to gain access to supporting information and underlying data readers are asked to contact the group via http://www.imperial.ac.uk/non-destructive-evaluation.

Acknowledgment

The authors would like to thank Prof. P. Cawley for discussions about the topic and suggestions about this paper. They would also like to thank Prof. R. Challis, Prof. M. Lowe, and Dr. P. Huthwaite for their comments on this paper.

References

[1] R. B. Thompson, "Physical principles of measurements with EMAT transducers," *Phys. Acoust.*, vol. 19, pp. 157–200, Dec. 1990.

[2] M. Hirao and H. Ogi, *EMATs for Science and Industry: Noncontacting Ultrasonic Measurements*. Norwell, MA, USA: Kluwer, 2003.

[3] K. S. Ho, T. H. Gan, D. R. Billson, and D. A. Hutchins, "Application of pulse compression signal processing techniques to electromagnetic acoustic transducers for noncontact thickness measurements and imaging," *Rev. Sci. Instrum.*, vol. 76, no. 5, p. 054902, 2005.

[4] E. R. Dobbs, "Electromagnetic generation of ultrasonic waves," in *Physical Acoustics*, vol. 10, W. P. Mason and R. N. Thurston, Eds. New York, NY, USA: Academic, 1973, pp. 89–127.

[5] P. Wilcox, M. Lowe, and P. Cawley, "Omnidirectional guided wave inspection of large metallic plate structures using an EMAT array," *IEEE Trans. Ultrason., Ferroelectr., Freq. Control*, vol. 52, no. 4, pp. 653–665, Apr. 2005.

[6] P. D. Wilcox, M. J. S. Lowe, and P. Cawley, "The excitation and detection of Lamb waves with planar coil electromagnetic acoustic transducers," *IEEE Trans. Ultrason., Ferroelectr., Freq. Control*, vol. 52, no. 12, pp. 2370–2383, Dec. 2005.

[7] X. Jian, S. Dixon, I. Baillie, R. S. Edwards, J. Morrison, and Y. Fan, "Shear wave generation using a spiral electromagnetic acoustic transducer," *Appl. Phys. Lett.*, vol. 89, no. 24, p. 244106, 2006.

[8] S. Wang, L. Kang, P. Xin, and G. Zhai, "Characteristic research and analysis of EMAT's transduction efficiency for surface detection of aluminum plate," in *Proc. 9th Int. Conf. Electron. Meas. Instrum. (ICEMI)*, Aug. 2009, pp. 4-949–4-955.

[9] S. Wang, P. Xin, L. Kang, and G. Zhai, "Research on influence of Lorentz force mechanism on EMAT's transduction efficiency in steel plate," in *Proc. 5th IEEE Conf. Ind. Electron. Appl. (ICIEA)*, Jun. 2010, pp. 196–201.

[10] R. Ribichini, F. Cegla, P. B. Nagy, and P. Cawley, "Study and comparison of different EMAT configurations for SH wave inspection," *IEEE Trans. Ultrason., Ferroelectr., Freq. Control*, vol. 58, no. 12, pp. 2571–2581, Dec. 2011.

[11] X. Chen, R. Su, H. Zhang, S. Wang, and G. Zhai, "Influence of coil parameters on transduction performance of unidirectional EMATs for Rayleigh wave," in *Proc. Far East Forum Nondestruct. Eval./Test., New Technol. Appl. (FENDT)*, Jun. 2013, pp. 150–154.

[12] M. Seher, P. Huthwaite, M. Lowe, P. Nagy, and P. Cawley, "Numerical design optimization of an EMAT for A_0 Lamb wave generation in steel plates," in *Proc. 40th Annu. Rev. Prog. Quant. Nondestruct. Eval., Incorp. 10th Int. Conf. Barkhausen Noise Micromagn. Test.*, 2014, vol. 1581. no. 1, pp. 340–347.

[13] P. B. Nagy, F. Simonetti, and G. Instanes, "Corrosion and erosion monitoring in plates and pipes using constant group velocity Lamb wave inspection," *Ultrasonics*, vol. 54, no. 7, pp. 1832–1841, 2014.

[14] A. Wilbrand, "EMUS-probes for bulk waves and Rayleigh waves. Model for sound field and efficiency calculations," in *New Procedures in Nondestructive Testing*. Berlin, Germany: Springer-Verlag, 1983, pp. 71–80.

[15] A. Wilbrand, "Quantitative modeling and experimental analysis of the physical properties of electromagnetic-ultrasonic transducers," in *Review of Progress in Quantitative Nondestructive Evaluation*, vol. 7, C. D. Thompson, Ed. New York, NY, USA: Plenum, 1987, pp. 671–678.

[16] R. Ribichini, F. Cegla, P. B. Nagy, and P. Cawley, "Experimental and numerical evaluation of electromagnetic acoustic transducer performance on steel materials," *NDT & E Int.*, vol. 45, no. 1, pp. 32–38, 2012.

[17] R. Ribichini, P. B. Nagy, and H. Ogi, "The impact of magnetostriction on the transduction of normal bias field EMATs," *NDT & E Int.*, vol. 51, pp. 8–15, Oct. 2012.

[18] R. Dhayalan, V. S. N. Murthy, C. V. Krishnamurthy, and K. Balasubramaniam, "Improving the signal amplitude of meandering coil EMATs by using ribbon soft magnetic flux concentrators (MFC)," *Ultrasonics*, vol. 51, no. 6, pp. 675–682, 2011.

[19] R. H. Koch, A. May, and J. Li, "Electromagnetic acoustic transducers for use in ultrasound inspection systems," U.S. Patent 7 426 867, Sep. 23 2008.

[20] B. Dutton, S. Boonsang, and R. J. Dewhurst, "Modelling of magnetic fields to enhance the performance of an in-plane EMAT for laser-generated ultrasound," *Ultrasonics*, vol. 44, pp. e657–e665, Dec. 2006.

[21] B. Dutton, S. Boonsang, and R. J. Dewhurst, "A new magnetic configuration for a small in-plane electromagnetic acoustic transducer applied to laser-ultrasound measurements: Modelling and validation," *Sens. Actuators A, Phys.*, vol. 125, no. 2, pp. 249–259, 2006.

[22] A. De Graff and M. De Waechter, "Elektrodynamischer Ultraschallwandler," DE Patent 4 011 686, Jul. 11, 1991.

[23] A. Graff and M. Wachter, "Electrodynamic ultrasonic transducer," U.S. Patent 5 148 414, Sep. 15, 1992.

[24] D. T. MacLauchlan, "Electromagnetic acoustic transducer (EMAT) for ultrasonic inspection of liquids in containers," U.S. Patent 5 837 898, Nov. 17, 1998.
[25] K. Mirkhani *et al.*, "Optimal design of EMAT transmitters," *NDT & E Int.*, vol. 37, no. 3, pp. 181–193, 2004.
[26] Z. Wang, W. H. Yang, X. B. Zhang, L. L. Hu, H. X. Wang, and Y. X. Zhang, "Design and manufacture of a near 3 T high field permanent magnet assembly," *IEEE Trans. Appl. Supercond.*, vol. 22, no. 3, Jun. 2012, Art. no. 4302304.
[27] C. Li and M. Devine, "Strong permanent magnet dipole with reduced demagnetizing effect," *IEEE Trans. Magn.*, vol. 45, no. 10, pp. 4380–4383, Oct. 2009.
[28] M. Kumada *et al.*, "Development of high field permanent magnet," *IEEE Trans. Appl. Supercond.*, vol. 12, no. 1, pp. 129–132, Mar. 2002.
[29] M. Kumada, E. I. Antokhin, Y. Iwashita, M. Aoki, and E. Sugiyama, "Super strong permanent dipole magnet," *IEEE Trans. Appl. Supercond.*, vol. 14, no. 2, pp. 1287–1289, Jun. 2004.
[30] *Introduction to the AC/DC Module*, COMSOL, Burlington, MA, USA, May 2013.
[31] *Permanent Magnets*, Hitachi Metals America, LLC, Arlington Heights, IL, USA, 2015.
[32] P. Rajagopal, M. Drozdz, E. A. Skelton, M. J. S. Lowe, and R. V. Craster, "On the use of absorbing layers to simulate the propagation of elastic waves in unbounded isotropic media using commercially available finite element packages," *NDT & E Int.*, vol. 51, pp. 30–40, Oct. 2012.
[33] X. Jian, S. Dixon, R. Edwards, K. Quirk, and I. Baillie, "Effect on ultrasonic generation of a backplate in electromagnetic acoustic transducers," *J. Appl. Phys.*, vol. 102, no. 2, p. 024909, 2007.

Julio Isla received the Engineering (*summa cum laude*) degree in telecommunications and electronics and the M.Sc. degree in radio-electronics from the Instituto Superior Polytechnic José Antonio Echeverría (ISPJAE), Havana, Cuba, in 2009 and 2012, respectively. He is currently pursuing the Ph.D. degree with the Non-Destructive Evaluation Group, Imperial College London, London, U.K.

He was with the Bioengineering Department, ISPJAE, from 2009 to 2011, and the Institute of Cybernetics, Mathematics and Physics, Havana, from 2011 to 2013. He has been with Permasense Ltd., Horsham, U.K., since 2014, a company that commercializes the low-power electromagnetic acoustic transducer technology that he developed with colleagues. He has also consulted for other international companies. His current research interests include low-power transduction, arrays, instrumentation, and signal processing.

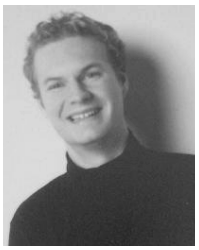

Frederic Cegla was born in Freiburg im Breisgau, Germany, in 1980. He received the M.Eng. and Ph.D. degrees in mechanical engineering from Imperial College London, U.K., in 2002 and 2006, respectively.

He was a Postdoctoral Research Fellow with the University of Queensland, Brisbane, Australia. In 2008, he started work at Imperial College London, as a Lecturer with the Dynamics Section, Mechanical Engineering Department, and in 2014, he was promoted to Senior Lecturer. He is a director of Permasense Ltd., a spin out company that exploits the high temperature wall thickness monitoring technology that has been developed by him and his colleagues. His current research interests include on the topics of high temperature ultrasonic monitoring, structural health monitoring, and ultrasonic manipulation of particles and bubbles.